Journal of Alloys and Compounds 736 (2018) 143–151

Contents lists available at ScienceDirect

Journal of Alloys and Compounds

journal homepage: http://www.elsevier.com/locate/jalcom

Silver-controlled evolution of morphological, structural, and optical properties of three-dimensional hierarchical WO_3 structures synthesized from hydrothermal method

L.F. Lopes [a], F.M. Pontes [a, *], L.O. Garcia [a], D.S.L. Pontes [a], D. Padovani [a], A.J. Chiquito [b], S.R. Teixeira [c], Y.N. Colmenares [d], V.R. Mastelaro [d], E. Longo [e]

[a] Department of Chemistry, Universidade Estadual Paulista - Unesp, P.O. Box 473, 17033-360, Bauru, São Paulo, Brazil
[b] NanO LaB, Department of Physics, Universidade Federal de São Carlos, Via Washington Luiz, Km 235, P.O. Box 676, 13565-905, São Carlos, São Paulo, Brazil
[c] Departamento of Physics, Universidade Estadual Paulista, Faculdade de Ciências e Tecnologia - FCT, Rua Roberto Simonsen, 305, 19060-900, Presidente Prudente, SP, Brazil
[d] Physics Institute of São Carlos (IFSC), University of São Paulo, São Carlos, SP, Brazil
[e] LIEC, CDMF- Department of Chemistry, Universidade Federal de São Carlos, Via Washington Luiz, Km 235, P.O. Box 676, 13565-905, São Carlos, São Paulo, Brazil

ARTICLE INFO

Article history:
Received 13 August 2017
Received in revised form
12 October 2017
Accepted 7 November 2017
Available online 9 November 2017

Keywords:
Tungsten oxide
Hydrothermal
Silver
Nanoparticles
Microcrystals

ABSTRACT

Hierarchical structures of self-assembled three-dimensional (3D) WO_3–Ag were synthesized via hydrothermal growth using precursor solutions of peroxopolytungstic acid with different amounts of Ag. The as-grown samples were analyzed by X-ray diffraction (XRD), field-emission scanning electron microscopy (FESEM), thermogravimetric analysis (TGA), Raman spectroscopy, Fourier transform infrared (FTIR) spectroscopy, ultraviolet–visible spectroscopy, and X-ray photoelectron spectroscopy. The XRD and Raman studies showed that as the amount of Ag was varied from 0 to 10 wt% in the hydrothermal growth solution, the crystal phase gradually changed from orthorhombic $WO_3 \cdot 0.33H_2O$ to hexagonal WO_3. The FTIR and TGA studies revealed different hydration levels, supporting the XRD and Raman results. By controlling the amount of Ag in the precursor solution, platelet-like building blocks and hexagonal building blocks were obtained, highlighting the role of Ag in the hydrothermal growth of 3D $WO_3 \cdot 0.33H_2O$ and WO_3 microcrystals. In addition, high-magnification FESEM images showed that the Ag nanoparticles were anchored on the surface of the 3D hierarchical WO_3–Ag structures, and the UV–vis measurements demonstrated that the 3D hierarchical structures gradually absorbed more light when the Ag content was increased. Moreover, the band-gap energy decreased when the Ag content was increased from 0 wt% (E_g = 2.65 eV) to 10 wt% (E_g = 2.26 eV). These experimental results demonstrate that the amount of Ag played a crucial role in determining the building blocks' morphology, and the hydration level, optical properties, and crystal phase of the $WO_3 \cdot nH_2O$ microcrystals.

1. Introduction

In the last few decades, crystal-growth engineering and technology (CGET) has been one of the main challenges in the design of semiconductor oxides. Several methods have been developed for the fabrication of these oxides, such as the co-precipitation method, sol–gel method, solvothermal method, hydrothermal method, microwave-assisted chemical route, spray drying, template-based technique, and inkjet printing [1–5].

Transition-metal semiconductor oxides represent a large family of materials with rich functionalities such as ferroeletricity, high electrical conductivity, transparency in visible light, colossal magneto-resistance, piezoelectricity, solar-energy harvesting capability, intelligent sensing, and optochromic and photocatalytical properties [6–11]. Recently, Lou et al. [12] explored the $FeNb_{11}O_{29}$ oxide as an alternative anode material for lithium-ion batteries. In addition, Liu et al. [13] reported the use $SrRuO_3$ perovkite oxide as an efficient counter electrode for dye-sensitized solar cells. Therefore, the effectiveness of a material in various applications highly depends on its size, shape, composition, and crystal phase. From this viewpoint, tungsten oxide (WO_3) has been

* Corresponding author.
E-mail address: fenelon@fc.unesp.br (F.M. Pontes).

https://doi.org/10.1016/j.jallcom.2017.11.095
0925-8388/

intensively studied, and there are different ways to tailor its chemical composition, morphology, size, and crystal phase [14–17]. In addition, the optical properties of WO_3 depend on the oxide crystal structure, and the energy gap is in the range of 2.6–3.5 eV [18,19]. For example, Ma et al. [20] reported that the urea content and solvent composition played important roles in controlling the shape and size of WO_3 nanostructures that were prepared using a template-free hydrothermal technique. Shi et al. [21] showed that $WO_3 \cdot nH_2O$ microcrystals with different shapes and crystal structures were successfully synthesized via the hydrothermal route by controlling the amount of inorganic salt, Na_2SO_4, in the precursor solution. In addition, there is great potential to manipulate the crystal-phase transformations of various WO_3 polymorphisms. Ahmadi et al. [22] studied the phase transformation from orthorhombic $WO_3 \cdot H_2O$ to monoclinic WO_3, which was initiated between 200 and 300 °C as a result of heat treatment. Santos and co-workers [23] demonstrated that the phase transformation from orthorhombic $WO_3 \cdot 0.33H_2O$ nanorods to monoclinic WO_3 nanoslabs occurred with increasing HCl concentration during hydrothermal synthesis. Wicaksana and co-workers [24] demonstrated that different morphologies and phases of WO_3 could be obtained by altering the concentration of sulfate (Na_2SO_4) and the pH level (H_2SO_4) in the hydrothermal method with $N_2WO_4 \cdot 2H_2O$ as precursor. Owing to these fascinating possibilities of crystal growth, massive efforts have been made to find and control different parameters that directly affect the size, shape, and crystal phases of materials on different length scales. In addition, special attention has been paid to hybrid heterostructures of noble metals (such as Au, Ag, and Pt) and WO_3 [25]. Ding and co-workers [26] reported selective deposition of Ag nanoparticles onto hexagonal WO_3 nanorods fabricated by a hybrid process involving hydrothermal treatment followed by in situ photo-reduction. Xing and co-workers [27] reported successful growth of Au nanoparticles anchored on the monoclinic surface of WO_3 nanorods after annealing at 500 °C for 2 h.

In the present work, we investigated the relationships between the size, shape, and phases of 3D WO_3 microcrystals with different amounts of silver, prepared using a one-step template-free hydrothermal route. The as-synthesized samples were characterized by X-ray diffraction (XRD), Fourier transform infrared (FTIR) spectroscopy, and Raman spectroscopy. The morphology of the samples was examined using field-emission scanning electron microscopy (FESEM) coupled with energy-dispersive X-ray (EDX) spectroscopy. Thermogravimetric analysis (TGA) was used to determine the weight loss of the as-synthesized samples. The oxidation states of tungsten and silver were determined by X-ray photoelectron spectroscopy (XPS). Furthermore, the optical properties of the samples were determined by ultraviolet–visible (UV–vis) spectroscopy.

2. Experimental procedure

All chemicals used in this work, such as tungstic acid (H_2WO_4), hydrogen peroxide (H_2O_2, 30%), and silver nitrate ($AgNO_3$), were analytical-grade reagents. First, a yellow solution was prepared by adding 0.375 g of H_2WO_4 to 10 mL of H_2O_2 and 30 mL of distilled water. The initially yellow solution discolored after it was mixed for 24 h with a magnetic stirrer, and a colorless solution of peroxopolytungstic acid complex was formed. Next, 0 (0 wt% Ag), 0.0059 g (1 wt% Ag), 0.0295 g (5 wt% Ag), or 0.059 g (10 wt% Ag) of an inorganic salt, $AgNO_3$, was dissolved in the colorless solution. The solution of complex peroxopolytungstic acid and $AgNO_3$ was then transferred to a 100 mL Teflon reaction vessel, and the rest of the vessel was filled with distilled water. Finally, the reaction vessel was placed in a stainless steel autoclave and heated at 200 °C for 2 h (hydrothermal growth solution method). After the hydrothermal treatment, the system was naturally cooled to room temperature, and the turbid suspension was centrifuged to collect the powder, which was washed thoroughly with deionized water several times to remove any unreacted precursors. Finally, the powder was dried in air at 70 °C for 1 h. After drying, white solids were obtained from the reaction mixtures containing 0 and 1% Ag, while yellow solids were obtained from the reaction mixtures containing 5 and 10% Ag. For simplicity, the powders derived from hydrothermal treatment of WO_3–0%Ag, WO_3–1%Ag, WO_3–5%Ag, and WO_3–10%Ag are hereafter referred to as W-0, W-1, W-5, and W-10, respectively.

The crystal structures were investigated by analyzing XRD patterns of Cu K_α radiation recorded by a diffractometer (Miniflex 600, Rigaku) in 2θ increments of 0.04°. The morphology of the samples was analyzed with an FESEM (Inspect F50, FEI) operated at an accelerating voltage of 5 kV. In addition, EDX spectroscopy was used in connection with FESEM for the elemental analysis. Raman spectra were recorded at room temperature using a spectrometer (Horiba) equipped with a Peltier-cooler charge-coupled device (Model HR 550). The samples were excited by a laser with wavelength of 532 nm. FTIR spectra were recorded in the 400–4000 cm^{-1} range using KBr pellets and an infrared spectrometer (FT/IR-4600, JASCO) with resolution of 4 cm^{-1} in the transmittance mode.

Thermal characterization was performed by thermogravimetry (TG) using a TG analyzer (SDT-Q600, TA Instruments). The analysis were carried out from room temperature to 1000 °C, at a heating rate of 10 °C/min, under an air flow of 100 mL/min, and using alumina cups. UV–vis spectra of the samples were obtained by a UV–vis spectrophotometer (Lambda 1050, PerkinElmer) equipped with an integrating sphere; MgO was used as the background reference material. XPS was conducted to study the elemental compositions and chemical states of the samples. The XPS spectra were obtained with a spectrometer system (ESCA+, Scienta-Omicron) equipped with a hemispherical analyzer (EA125) and a monochromated Al K_α (Xm1000, 1486.7 eV) radiation source. In order to compensate for the charge effect in the sample, a charge neutralizer (CN10, Omicron) with beam energy of 1.6 eV was used. During the analysis, the chamber was evacuated to 2×10^{-9} Pa, and the energy steps were 50 and 20 eV for the survey and high-resolution spectra, respectively. The peak fitting was performed using a 70% Gaussian curve, a 30% Lorentzian curve, and a Tougaard nonlinear sigmoid baseline. The C 1s peak of adventitious carbon was fixed at 284.8 eV to set the scale of the binding energy, and the data fitting was performed using CasaXPS software (Casa Software Ltd., UK).

3. Results and discussion

X-ray diffraction patterns were analyzed to investigate the degree of crystallinity and phase transformation of the final product derived from hydrothermal treatment of WO_3 at 200 °C for 2 h in the presence of different amounts of Ag. Fig. 1 shows XRD patterns of four samples (W-0, W-1, W-5, and W-10) prepared in the presence of 0, 1, 5, and 10 wt% of Ag. All main peaks in the XRD patterns are very strong and narrow, suggesting that the as-synthesized samples had high crystallographic quality. In addition, no significant signals of silver or its oxide compounds were detected, probably because of the relatively low amount and very small size of Ag nanoparticles. In fact, part of the unreacted silver may have been removed during the washing process, and similar results have been reported in the literature [28–30]. All diffraction peaks in the XRD patterns of samples W-0 and W-1 can be exclusively indexed by the orthorhombic $WO_3 \cdot 0.33H_2O$ phase with lattice parameters of a = 7.342 Å, b = 12.552 Å, and c = 7.695 Å (JCPDS Card No.

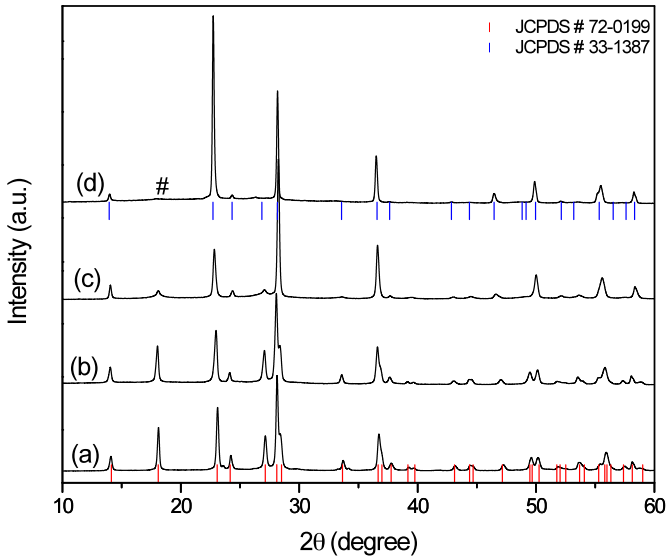

Fig. 1. XRD patterns of pure WO_3 and WO_3–Ag with different amounts of Ag after hydrothermal treatment at 200 °C for 2 h: (a) W-0; (b) W-1; (c) W-5; (d) W-10. Standard patterns of orthorhombic $WO_3 \cdot 0.33H_2O$ (red solid line) and hexagonal WO_3 (blue solid line). (For interpretation of the references to colour in this figure legend, the reader is referred to the web version of this article.)

72–0199). However, the XRD patterns show that the hexagonal phase gradually became dominant with increasing Ag content. Moreover, a mixture of hydrated orthorhombic and hexagonal phases was observed in sample W-5, but a primarily hexagonal phase of the WO_3 structure was observed in sample W-10. In the last case, lattice parameters of $a = 7.781$ Å and $c = 3.808$ Å (JCPDS Card No. 33–1387) and a strong preferential growth direction along the *c* axis [001] were found for sample W-10, as clearly indicated by the XRD pattern in Fig. 1(d). Furthermore, close observation revealed a very small fraction of the orthorhombic $WO_3 \cdot 0.33H_2O$ phase (labeled by the symbol # in Fig. 1(d)). These changes in the crystal structure indicate that the amount of Ag played an important role in the phase transformation, degree of hydration, and stabilization of the type of crystal structure. Therefore, it can be concluded that different phases of $WO_3 \cdot nH_2O$ were generated as the amount of Ag in the hydrothermal growth solution was gradually increased. Balazsi and Pfeiter [31] also demonstrated that the dehydration degree of hydrated tungsten oxide is very sensitive to the amount of sodium ions during hydrothermal treatment. This observation is also supported by different works, which suggested that the degree of hydration, morphology, and crystal structure of tungsten oxide are very sensitive to the concentration of precursor solutions such as HCl, NH_4Cl, NH_4NO_3, $(NH_4)_2SO_4$, Li_2SO_4, and Na_2SO_4 [32–35].

One possible explanation of these observations is presented as follows. The silver ions acting as a structure-directing agent altered the nucleation and growth mechanisms of WO_3 crystals, resulting in the formation of interstructural hydrogen bonds between layers of WO_3 during the hydrothermal route. In the absence of Ag, the dissolution and recrystallization processes of the peroxopolytungstic acid precursor solution occurred naturally under the same hydrothermal conditions (equations (1) and (2)):

$$WO_4^{2-} + 2H_3O^+ + nH_2O \rightarrow H_2WO_4 \cdot nH_2O, \quad (1)$$

$$H_2WO_4 \cdot nH_2O \rightarrow (WO_3) \cdot nH_2O. \quad (2)$$

When the inorganic salt $AgNO_3$ was added to the hydrothermal growth solution, the Ag^+ ions changed the growth environment of the initial WO_4^{2-} and H_3O^+ building blocks in the peroxopolytungstic acid precursor solution. Furthermore, the interaction between Ag^+ ions and WO_4^{2-} building blocks in the hydrothermal growth solution resulted in the transfer of electrons to Ag^+ and the release of water molecules (equations (3) and (4)):

$$WO_4^{2-} + 2H_3O^+ + Ag^+ \rightarrow WO_3 + Ag + 3H_2O, \quad (3)$$

$$2H_3O^+ + O^{2-} \rightarrow 3H_2O. \quad (4)$$

When the concentration of Ag^+ ions in the hydrothermal growth solution was increased (equations (3) and (4)), causing the dehydration of WO_4^{2-} building blocks, bond breaking and formation of new bonds are expected. This dynamical process led to a new and stable structure, namely, hexagonal anhydrous tungsten oxide (see Fig. 1(d)).

Raman spectroscopy was also performed to investigate the phase transformation from orthorhombic $WO_3 \cdot 0.33H_2O$ to hexagonal WO_3 in samples W-0, W-1, W-5, and W-10. The spectra of all crystalline tungsten oxide samples can be divided into four main regions—above 900 cm^{-1}, between 900 and 600 cm^{-1}, between 400 and 200 cm^{-1}, and below 200 cm^{-1}—assigned to various stretching, bending, and lattice modes [36–38]. As depicted in Fig. 2, the Raman spectra of samples W-0 and W-1 show the formation of the orthorhombic $WO_3 \cdot 0.33H_2O$ crystal phase. The small intensity bands at 946 and 921 cm^{-1} correspond to stretching vibrations of terminal W=O and W–O bonds, respectively [39]. The bands located at 802 and 685 cm^{-1} can be attributed to stretching vibrations of O–W–O, while the weak shoulder at 629 cm^{-1} can be attributed to the vibration of bridging oxygen atoms [40]. The weak peak at 470 cm^{-1} may be associated with the vibration of water molecules. The Raman modes located around 337 and 266 cm^{-1} could have originated from the bending vibrations of W–O–W [41]. In addition, the bands located around 195, 166, and 76 cm^{-1} are attributed to the lattice vibrations [38,42]. Additionally, samples W-5 and W-10 exhibited distinct spectral bands that showed drastically intensity changes, suggesting a local structural change. Upon comparison of the stretching, bending and lattice vibrational modes of samples W-0, W-1, W-5, and W-10, the wavenumbers were found to shift towards higher and lower values as the Ag content was increased. For example, the major vibrational modes

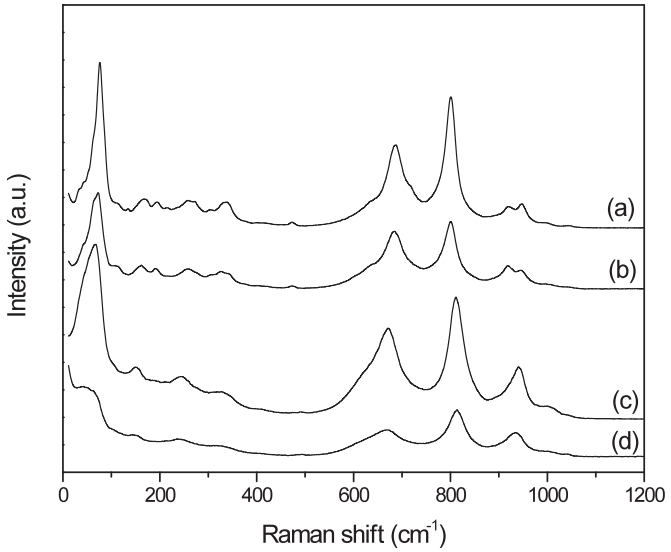

Fig. 2. Raman spectra of pure WO_3 and WO_3–Ag with different amounts of Ag after hydrothermal treatment at 200 °C for 2 h: (a) W-0; (b) W-1; (c) W-5; (d) W-10.

located at 802, 685, and 76 cm^{-1} for the orthorhombic $WO_3 \cdot 0.33H_2O$ phase of sample W-0 were shifted to 815, 667, and 46 cm^{-1} in the spectrum of sample W-10. These bands are characteristic features of the hexagonal WO_3 crystal phase. Interestingly, increases in Ag content (samples W-5 and W-10) generated changes in the region characterized by stretching vibrations of terminal W═O and W–O bonds. The bands located at 946 and 921 cm^{-1} corresponding to the orthorhombic $WO_3 \cdot 0.33H_2O$ phase overlap, and only one band appears at 936 cm^{-1} in the spectra of samples W-5 and W-10. These results further confirm the presence of the hexagonal WO_3 phase (Fig. 2(c) and (d)). Similar vibrational modes were also reported by Sing et al. [43].

Therefore, both Raman and XRD results confirm the conversion from orthorhombic $WO_3 \cdot 0.33H_2O$ to hexagonal WO_3 crystal structure with increasing Ag content.

In addition, the structural and functional groups present in the as-synthesized samples were determined by FTIR spectral analysis, see Fig. 3. It has been reported that the orthorhombic $WO_3 \cdot 0.33H_2O$ crystal structure consists of layered stacks of $WO_5(OH_2)$ octahedra and interlayer water molecules [44–46]. For orthorhombic $WO_3 \cdot 0.33H_2O$, the interlayer water molecules connected the $WO_5(OH_2)$ octahedra planes through hydrogen bonds [46]. The FTIR spectrum of sample W-0 shows vibrational bands located at 3494 and 3470 cm^{-1} that are usually attributed to –OH and H_2O stretching vibrations, while an additional sharp band due to structural water molecules appears at 1606 cm^{-1} (Fig. 3(a)). The bands located at 994 and 954 cm^{-1} are assigned to the stretching mode of the terminal W═O bond, which is very common for the orthorhombic $WO_3 \cdot 0.33H_2O$ phase. Furthermore, a very strong and broad band between 813 and 730 cm^{-1} and a shoulder at 665 cm^{-1} can be ascribed to O–W–O stretching vibrations. The presence of these absorption peaks was attributed to the high degree of sample W-0 crystallinity. A similar spectrum was recorded for sample W-1, with shoulders at 813 and 665 cm^{-1} and a very strong band at 734 cm^{-1}. All the bands observed in samples W-0 and W-1 can be attributed exclusively to the orthorhombic $WO_3 \cdot 0.33H_2O$ phase, which are in good agreement with the work by Daniel et al. [38]. As previously reported in the literature, the crystalline orthorhombic $WO_3 \cdot 0.33H_2O$ structure is mainly formed by two types of WO_6 octahedra: one of them is formed exclusively by W–O bonds, and the other by W═O and $W–OH_2$ terminal bonds and four oxygen atoms on the *a*–*b* plane [47,48]. Thus, these bands should be strongly affected by the dehydration level of $WO_3 \cdot 0.33H_2O$. As expected, the $W–OH\cdots H_2O$, W–OH, and W═O vibration modes were strongly affected, as shown in the spectra of samples W-5 and W-10 (Fig. 3(c) and (d), respectively). The $W–OH\cdots H_2O$ and W–OH stretching vibrations, which were related to adsorbed and crystal water molecules represented by peaks at around 3440 and 1606 cm^{-1}, respectively, showed an appreciable decrease in intensity. This suggests that a high degree of dehydration took place as the amount of Ag was increased under hydrothermal growth conditions, inducing rearrangement of local atoms and the formation of more symmetric WO_6 polyhedra. In addition, the bands at 994 and 954 cm^{-1}, which correspond to W═O stretching vibrations, are completely absent in the spectra of samples W-5 and W-10 (Fig. 3(c) and (d), respectively), while the bands corresponding to O–W–O triplet stretching (600–900 cm^{-1}) in the spectra of samples W-0 and W-1 merge to form a single band located at 698 cm^{-1}. This suggests the conversion from orthorhombic $WO_3 \cdot 0.33H_2O$ to hexagonal WO_3. Similar modes in hexagonal WO_3 nanowires were reported by Phuruangrat et al. [25]. Choopool et al. [49] also summarized the vibrational modes in tungsten oxide nanoflowers, whose strong absorption band around 660 cm^{-1}, assigned to O–W–O vibrations, suggests the formation of hexagonal WO_3. Again, our FTIR results indicate a decrease in the degree of hydration of samples upon an increase in Ag content, as well as a rearrangement of local atoms and conversion of part of the W═O and $W–OH_2$ bonds to O–W–O bonds.

The TG curves of the samples, illustrated in Fig. 4, clearly display characteristic stepwise weight loss due to the dehydration reaction of the as-synthesized samples [50,51]. For sample W-0, weight loss started at 30 °C and continued until the temperature reached 450 °C. The total weight loss was found to be around 3.84 wt%, which is higher than the theoretically calculated value (2.52%) for $0.33H_2O$ molecule in the orthorhombic $WO_3 \cdot 0.33H_2O$ phase. The observed weight loss thus suggests that besides the structurally coordinated water molecules, sample W-0 also contained high amounts of physisorbed water molecules. The TG curve of sample W-1 shows a total weight loss of around 3.66 wt%, attributed to physisorbed water molecules and the removal of structurally coordinated water molecules. The total weight loss of sample W-5 was around 3.37%: the slight weight loss between 30 and 180 °C can be attributed to the low amount of adsorbed water on the sample

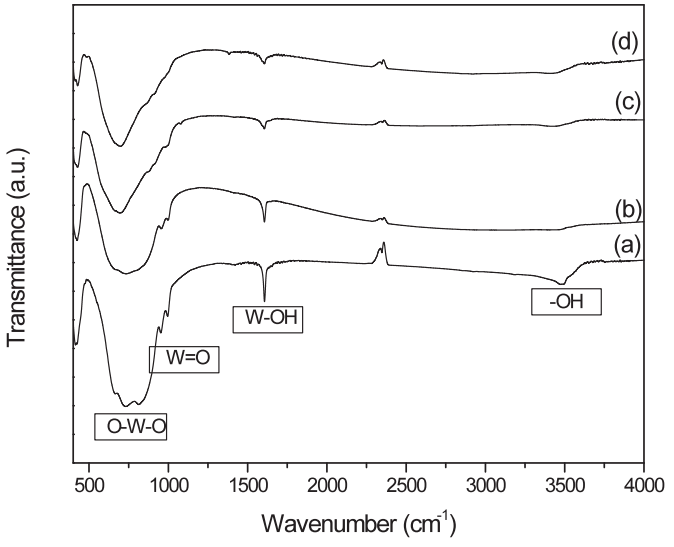

Fig. 3. Room-temperature FTIR spectra of pure WO_3 and WO_3–Ag samples prepared from hydrothermal growth solutions containing different amounts of Ag: (a) W-0; (b) W-1; (c) W-5; (d) W-10.

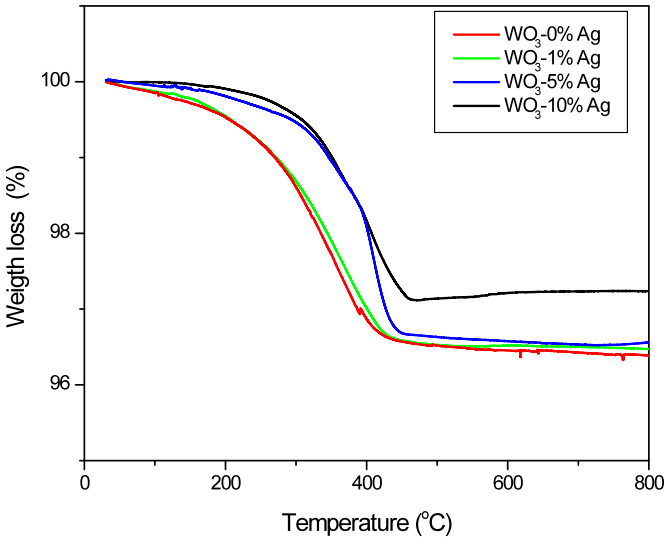

Fig. 4. TGA of as-synthesized products prepared from hydrothermal growth solutions containing different amounts of Ag: (a) W-0; (b) W-1; (c) W-5; (d) W-10.

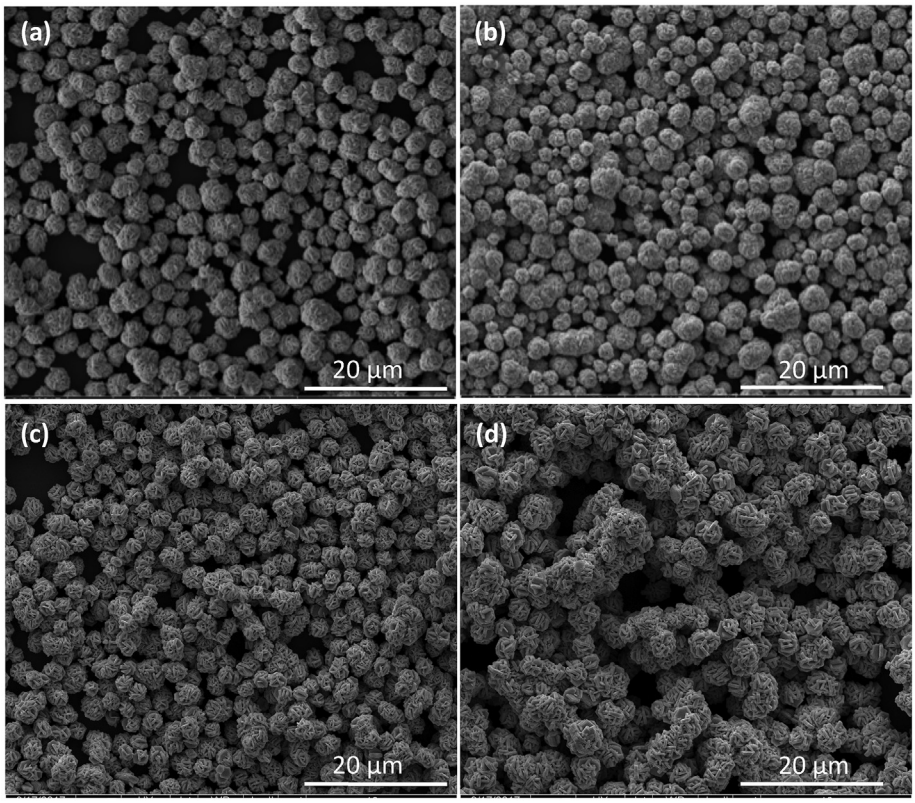

Fig. 5. Low-magnification FESEM images of final products obtained after hydrothermal treatment at 200 °C for 2 h in the presence of different amounts of Ag: (a) W-0; (b) W-1; (c) W-5; (d) W-10.

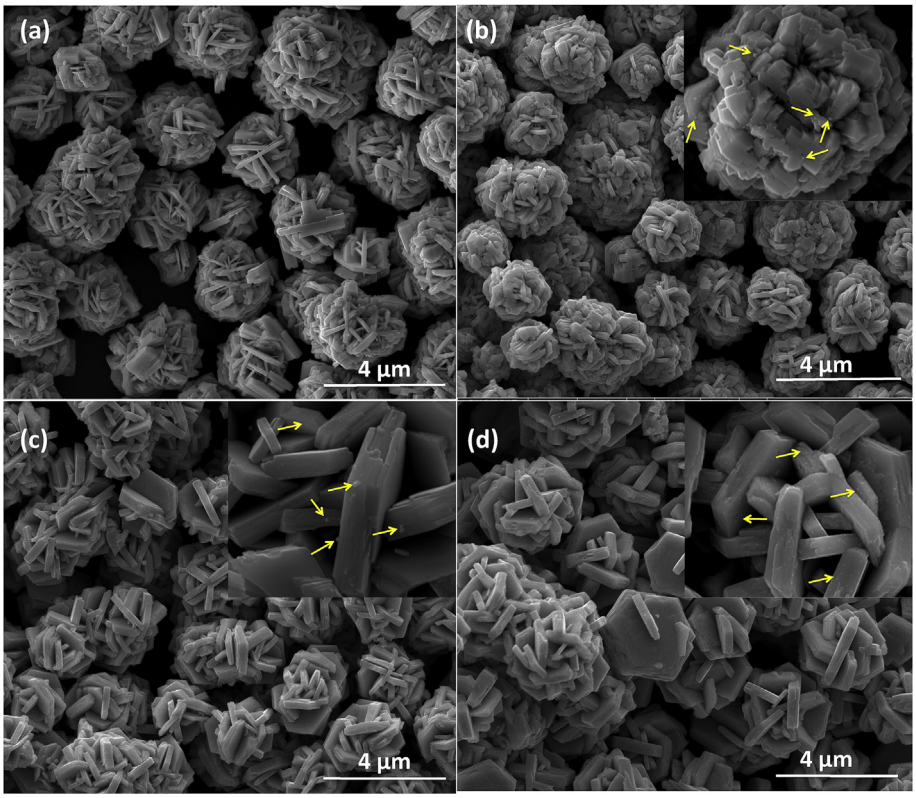

Fig. 6. High-magnification FESEM images of final products obtained after hydrothermal treatment at 200 °C for 2 h in the presence of different amounts of Ag: (a) W-0; (b) W-1; (c) W-5; (d) W-10. The inset shows a close-up image of Ag nanoparticles (indicated by the yellow arrow) anchored on the surface of 3D hierarchical microcrystals. (For interpretation of the references to colour in this figure legend, the reader is referred to the web version of this article.)

surface; the distinct weight loss that occurred between 180 and 450 °C indicates the removal of hydration water from the orthorhombic $WO_3 \cdot 0.33H_2O$ phase, confirming the XRD and FTIR results. Unlike samples W-0, W-1, and W-5, sample W-10 displays a flat region between 30 and 180 °C in its TG curve. Practically no weight loss occurred in sample W-10 until 180 °C, suggesting the absence (or a very small amount) of physisorbed water molecules. Moreover, the weight loss of 2.84% observed between 180 and 480 °C was due to the removal hydration water, showing that sample W-10 could have contained a very small fraction of the orthorhombic $WO_3 \cdot 0.33H_2O$ phase, which is also in good agreement with the XRD results.

The as-synthesized tungsten oxide samples were also examined by FESEM to explore their shape and size. Low-magnification FESEM images of samples W-0, W-1, W-5, and W-10 revealed a spherical morphology with mean sizes of 2.0, 2.0, 2.5, and 2.7 μm, respectively, as depicted in Fig. 5. Close inspection of the image of sample W-0 in Fig. 6(a) revealed a microstructure that was self-organized into a hierarchical spherical flower-like superstructure comprising large interleaving irregular platelet-like structures. Fig. 6(b) reveals that sample W-1 also shows a more compact hierarchical spherical morphology comprising larger irregular wedge-like structures serving as building blocks. The high-magnification FESEM image in the inset of Fig. 6(b) clearly shows very small Ag nanoparticles (size: 5–8 nm) anchored on the larger wedge-like structures of the orthorhombic $WO_3 \cdot 0.33H_2O$ phase. In contrast, as the amount of Ag increased, as in samples W-5 and W-10 (Fig. 6(c) and (d), respectively), one can clearly see that the hierarchical spherical flower-like superstructures were self-assembled from large amounts of intercrossed hexagonal platelet-like structures in all directions. In Table 1 there is a comparison between our $WO_3 \cdot Ag$ morphology results and other preparation methods. In addition, the high-magnification FESEM images in the insets of Fig. 6(c) and (d) show Ag nanoparticles anchored on the hexagonal WO_3 phase. Again, these observations indicate that Ag^+ ions influenced the crystallization of the hexagonal phase of WO_3. The positively charged initial clusters, $[Ag(OH_2)_6]^+$, interacted with the $WO_6 \cdot 2H_3O$ clusters, replacing the H_3O^+ ion, thus neutralizing the negative charges of WO_6^{3-}. This replacement led to the dehydration of these clusters, thus allowing the formation of dehydrated surfaces. These surfaces then interacted to form different crystallographic planes, which grew in directions that were different from those of the hydrated clusters, resulting in a new crystallographic symmetry. Based on the experimental results, a simple schematic growth mechanism of the 3D hierarchical spherical microstructures is proposed and illustrated in Fig. 7. The EDX spectra of the samples, shown in Fig. 8, indicate that the increase in the amount of Ag on tungsten oxide was followed by a corresponding increase in the Ag peak intensity, confirming the presence of Ag in the as-synthesized material. Furthermore, the EDX spectra confirm that the samples contained only the elements W, O, and Ag, and no impurities were observed.

UV–vis diffuse reflectance measurements were carried out to evaluate the optical properties of the as-synthesized tungsten oxide samples. As depicted in Fig. 9(a), the absorption edge gradually red-shifted towards longer wavelengths as the Ag amount was increased, revealing the strong interaction between Ag nanoparticles and tungsten oxide. At the same time, when compared

Table 1
A summary of WO_3 materials prepared by different methods.

Synthesis route	Morphology	References
Solvothermal	Nanoparticles	64
Hydrothermal	hexagonal disc-like	47
Hydrothermal	Nanowires	59
Hydrothermal	Nanorods	58
Soft chemistry route	Nanoparticles	63
Pulsed plasma in liquid	Nanoparticles	62
Microwave oven	Nanoparticles	54
Cationic surfactant route	3D flower-like microspheres	42
Chemical precipitation	Disc-shaped	60
Chemical exfoliation	Nano-sheets	61
Wet chemical method	Nanoplatelets	36
Hydrothermal[a]	3D flower-like microspheres	

[a] This work.

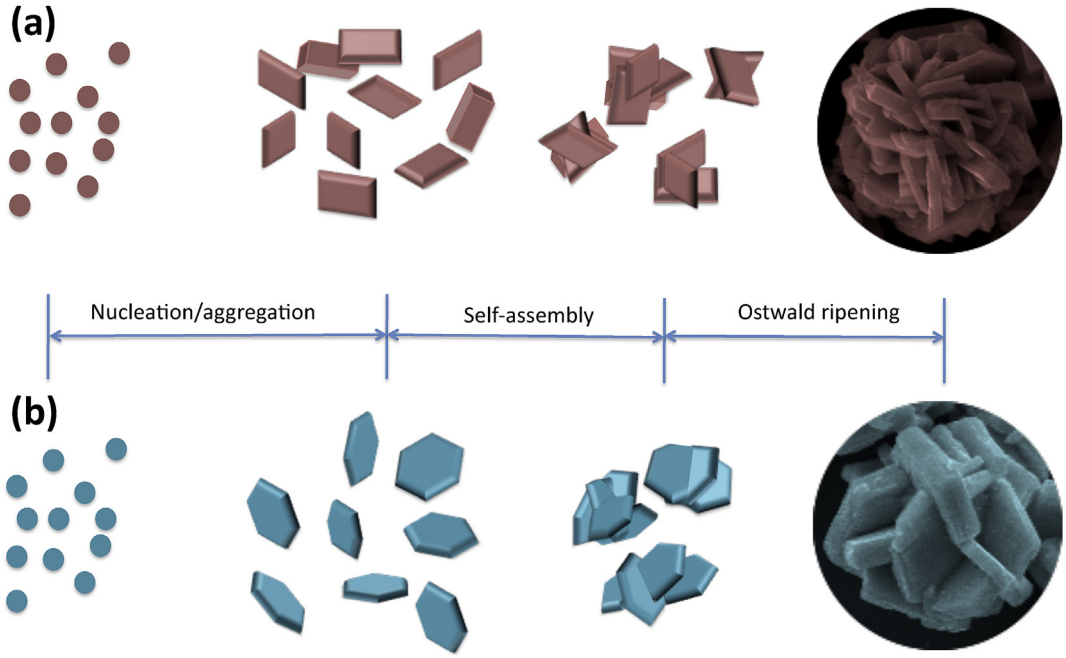

Fig. 7. Schematic illustration of the formation mechanism of 3D hierarchical $WO_3 \cdot nH_2O$ microcrystals prepared from hydrothermal solutions containing different amounts of Ag: (a) 0 < Ag < 1 wt%; (b) 5 wt% < Ag < 10 wt%.

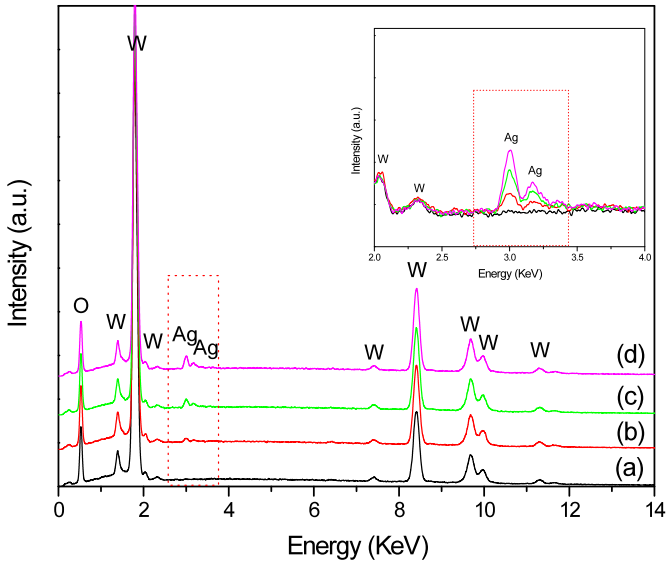

Fig. 8. EDX spectra of pure WO_3 and WO_3–Ag with different amounts of Ag after hydrothermal treatment at 200 °C for 2 h: (a) W-0; (b) W-1; (c) W-5; (d) W-10. The inset shows a close-up view of the Ag signal.

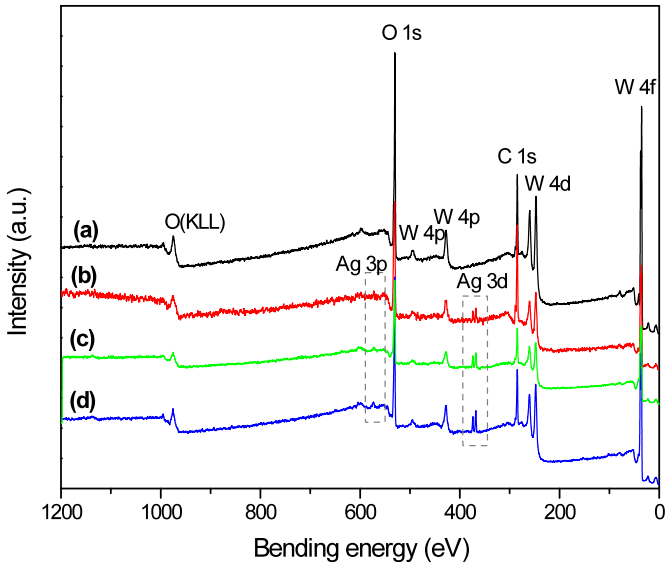

Fig. 10. Typical survey XP spectra of pure WO_3 and WO_3–Ag with different amounts of Ag: (a) W-0; (b) W-1; (c) W-5; (d) W-10.

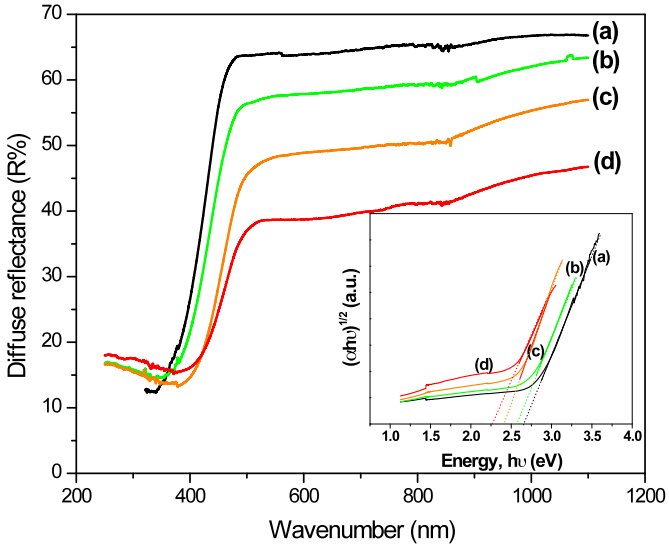

Fig. 9. The UV–vis diffuse reflection spectra of pure WO_3 and WO_3–Ag with different amounts of Ag after hydrothermal treatment at 200 °C for 2 h: (a) W-0; (b) W-1; (c) W-5; (d) W-10. The inset shows plots of $(\alpha h\nu)^{1/2}$ versus photon energy ($h\nu$) and plots of the band-gap energy.

with samples W-0, W-1, and W-5, the high amount of Ag on tungsten oxide was responsible for the high light absorption of sample W-10 in the visible-light region. The behavior observed in Fig. 9(a) also suggests that the gradual increase in light absorption can be attributed to the localized surface-plasmon resonance (LSPR) of Ag nanoparticles, as previously reported by Ding et al. and Ren et al. [26,52]. In addition, the band-gap energies of the as-synthesized samples were estimated by the well-known Tauc equation [53]. Based on the plot of $(\alpha h\nu)^{1/2}$ versus $h\nu$, the band-gap energies of samples W-0, W-1, W-5, and W-10 were estimated to be 2.65, 2.56, 2.35, and 2.26 eV, respectively (inset in Fig. 9(b)). Remarkably, this decrease in band-gap energy was related to the amount of Ag: the presence of Ag nanoparticles could introduce new discrete energy levels to the band gap of WO_3, making it increasingly narrow as a result. This finding is also in agreement with results of other studies in which a decrease in band-gap energy was observed for metal-load tungsten oxide [27,53–56].

The chemical compositions and states of the as-synthesized products were further investigated using XPS. The survey spectra in Fig. 10 indicate that in addition to adventitious carbon, all as-synthesized samples consisted mainly of tungsten, oxygen, and silver. The high-resolution XPS spectra recorded in the region of W 4f for all as-synthesized samples show the W $4f_{7/2}$ and W $4f_{5/2}$ doublet located at 35.2 and 37.4 eV, respectively. These energies are associated with W^{6+} ions (Fig. 11(a)) [55,57]. The high-resolution XPS O 1s spectra were deconvolved into three peaks (Fig. 11(b)): the main peak at the lowest binding energy originated from the W–O bond in the WO_3 lattice [15,48]; the second peak, with weak intensity at about 531 eV, corresponds to the existence of the hydroxyl group, i.e., the –OH bond, and it originated from adsorbed or interstructural water molecules [22]; the third peak at the highest binding energy of ~533 eV corresponds to the C–O bonds representing adventitious carbon detected in the survey spectrum [22]. Fig. 10(c) presents the high-resolution XPS Ag 3d spectra of samples W-1, W-5, and W-10: the peaks are assigned to the binding energies of Ag $3d_{3/2}$ and Ag $3d_{5/2}$, with values of about 372.8 and 366.8 eV (W-1), 373.8 and 367.7 eV (W-5), and 373.2 and 367.2 eV (W-10) [26,42,56]. The XPS results, based on the binding energies of the Ag 3d level of samples W-1, W-5, and W-10, suggest that Ag was partially oxidized to Ag_2O. However, we cannot rule out the presence of Ag_2O in favor of metallic Ag because there was no appreciable shift in the binding energy between them.

4. Conclusion

WO_3–Ag samples were prepared from peroxopolytungstic acid precursor solutions followed by hydrothermal treatment in an aqueous solvent with different amounts of Ag. Our results suggest that the crystal structure, visible-light absorption properties, and morphology of WO_3 can be tuned by adding Ag during the hydrothermal treatment. The XRD, Raman, FTIR, and FESEM results confirmed that there were different crystallographic structures and building blocks in the hierarchical architecture of WO_3–Ag microspheres with increasing Ag content. The FESEM images revealed

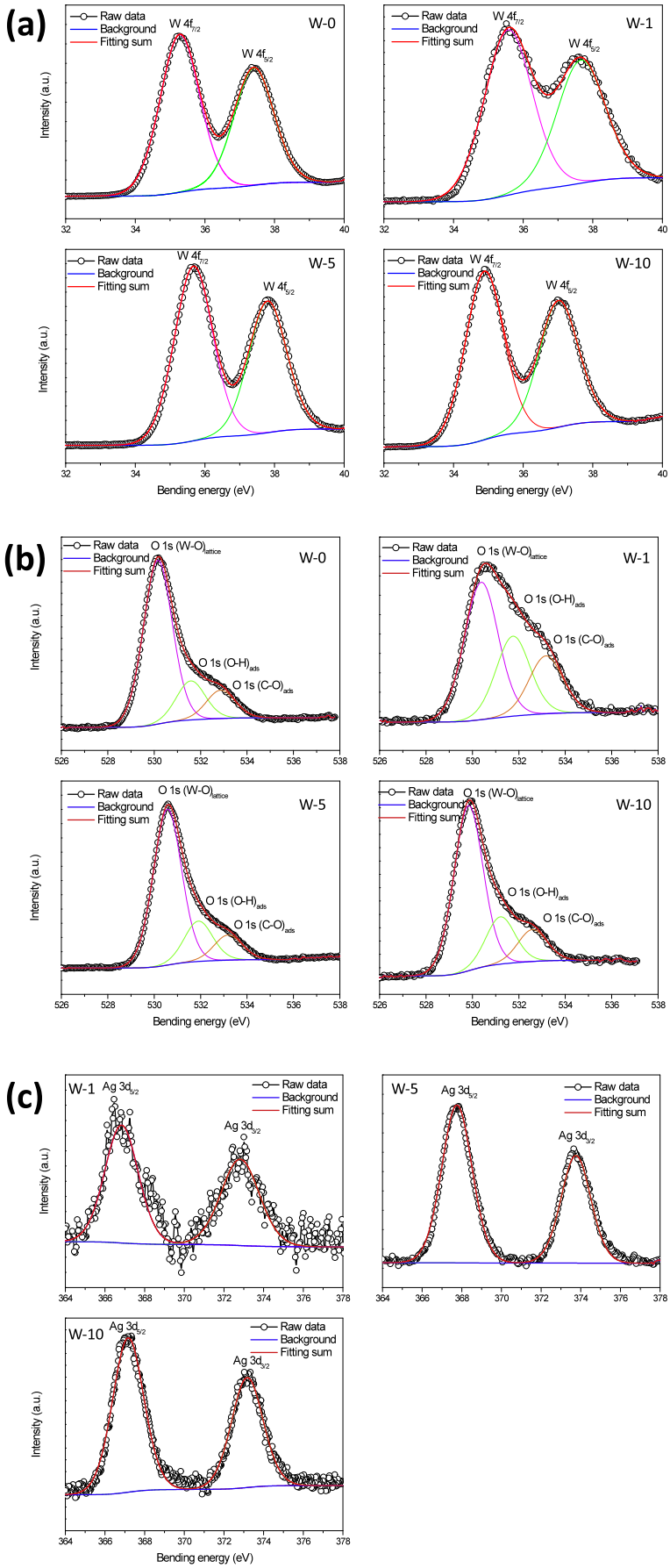

Fig. 11. High-resolution XP spectra of pure WO_3 and WO_3–Ag with different amounts of Ag: (a) core-level spectra of W 4f; (b) core-level spectra of O 1s; (c) core-level spectra of Ag 3d.

Ag nanoparticles (5–8 nm) anchored on the WO_3 surface. The XRD, Raman, and FTIR results revealed that a phase transformation from orthorhombic $WO_3 \cdot 0.33H_2O$ to hexagonal WO_3 took place at higher Ag concentrations. Furthermore, FESEM images revealed that the 3D hierarchical structures of spherical building blocks evolved with increasing Ag content from platelet-like hierarchical structures for samples with low Ag content ($0\% < x < 1\%$) to hexagonal hierarchical structures for those with high Ag content ($5\% < x < 10\%$). It was clear that the amounts of Ag^+ and NO_3^- ions played important roles in the formation of such structures. The FTIR and TGA results showed that different degrees of hydration were obtained as the Ag content was increased from 1 to 10 wt%. The XPS studies showed the presence of W^{6+} ions in all as-synthesized samples, while a more detailed core-level XPS study confirmed the presence of Ag in partially oxidized states. It was also found that the optical band-gap energy of 3D hierarchical tungsten oxide structures gradually decreased with increasing Ag content.

Acknowledgments

This study was financially supported by the Brazilian agencies FAPESP and CNPq. In particular, we would like to acknowledge CEPID/CMDMC/INCTMN/CDMF, FAPESP processes no. 11/20536-7, 12/14106-2, and 13/07296-2 and CNPq process no. 470147/2012-1.

References

[1] P.R. Sajanlal, T.S. Sreeprasad, A.K. Samal, T. Pradeep, Nano Rev. 2 (2011) 1–62.
[2] D.G. Shchukin, G.B. Sukrorukov, Adv. Mater. 16 (2004) 671–682.
[3] J.Y. Zheng, Z. Haider, T.K. Van, A.U. Pawar, M.J. Kang, C.W. Kim, Y.S. Kang, CrystEngComm 17 (2015) 6070–6093.
[4] J. Li, J. Huang, J. Wu, L. Cao, Q. Li, K. Yanagisawa, CrystEngComm 15 (2013) 7904–7913.
[5] H. Hossainian, M. Salavati-Niasari, M. Bazarganipour, J. Mol. Liq. 220 (2016) 747–754.
[6] J.B. Cai, X.Q. Wu, S. Li, F. Zheng, ACS Sustain. Chem. Eng. 4 (2016) 1581–1590.
[7] S.S. Patil, M.G. Mali, M.S. Tamboli, D.R. Patil, M.V. Kulkarni, et al., Catal. Today 260 (2016) 126–134.
[8] C. Alippi, CAAI Transactions on Intelligence Technology, vol. 1, 2016, pp. 1–3.
[9] X. Zhang, H. Gao, M. Guo, G. Li, Y. Liu, D. Li, CAAI Transactions on Intelligence Technology, vol. 1, 2016, pp. 4–13.
[10] H. Jin, Q. Chen, Z. Chen, Y. Hu, J. Zhang, CAAI Transactions on Intelligence Technology, vol. 1, 2016, pp. 104–113.
[11] S. Zinatloo-Ajabshir, M.S. Morassaei, M. Salavati- Niasari, J. Colloid Interface Sci. 497 (2017) 298–308.
[12] X. Lou, C. Lin, Q. Luo, J. Zhao, B. Wang, J. Li, Q. Shao, X. Guo, N. Wang, Z. Guo, ChemElectroChem. (2017), https://doi.org/10.1002/celc.201700816.
[13] T. Liu, K. Yu, L. Gao, H. Chen, N. Wang, L. Hao, T. Li, H. He, Z. Guo, J. Mater. Chem. 5 (2017) 17848–17855.
[14] S. Cao, H. Chen, J. Alloy. Comp. 702 (2017) 644–648.
[15] A. Yan, C. Xie, F. Huang, S. Zhang, S. Zhang, J. Alloy. Comp. 610 (2014) 132–137.
[16] P.J. Wojcik, L. Santos, L. Pereira, R. Martins, E. Fortunato, Nanoscale 7 (2015) 1696–1708.
[17] T. Peng, D. Ke, J. Xiao, L. Wang, J. Hu, L. Zan, J. Solid State Chem. 194 (2012) 250–256.
[18] H.J. Yuan, Y.Q. Chen, F. Yu, Y.H. Peng, X.W. He, D. Zhao, D.S. Tang, Chin. Phys. B 20 (2011) 36103(1)–36103(6).
[19] H. Zheng, J.Z. Ou, M.S. Strano, R.B. Kaner, A. Mitchell, K. Kalantar-zadeh, Adv. Funct. Mater. 21 (2011) 2175–2196.
[20] D. Ma, G. Shi, H. Wang, Q. Zhang, Y. Li, Mat. Chem. A 1 (2013) 684–691.
[21] J. Shi, G. Hu, R. Cong, H. Bu, N. Dai, New J. Chem. 37 (2013) 1538–1544.
[22] M. Ahmadi, R. Younesi, M.J.F. Guinel, J. Mater. Res. 29 (2014) 1424–1430.
[23] L. Santos, P. Wojcik, J.V. Pinto, E. Elangovan, J. Viegas, L. Pereira, R. Martins, E. Fortunato, Adv. Electron. Mater 1 (2015) 1400002–1400010.
[24] Y. Wicaksana, S. Liu, J. Scott, R. Amal, Molecules 19 (2014) 17747–17762.
[25] M.G.C. Zoontjes, M. Huijben, J. Baltrusaitis, W.G. van der Wiel, G. Mul, Appl. Mater. Interfaces 5 (2013) 13050–13054.
[26] J. Ding, Y. Chai, Q. Liu, X. Liu, J. Ren, W.L. Dai, J. Phys. Chem. C 120 (2016) 4345–4353.
[27] Q. Xiang, G.F. Meng, H.B. Zhao, Y. Zhang, H. Li, W.J. Ma, J.Q. Xu, J. Phys. Chem. C 114 (2010) 2049–2055.
[28] W. Zhu, J. Liu, S. Yu, Y. Zhou, X. Yan, J. Hazard Mater. 318 (2016) 407–416.
[29] Z. Wu, X. Lü, X. Wei, J. Shen, J. Xie, J. Mater. Res. 29 (2014) 71–80.
[30] S. Ghosh, S.S. Acharyya, T. Sasaki, R. Bal, Green Chem. 17 (2015) 1867–1876.
[31] C. Balazsi, J. Pfeifer, Solid State Ionics 151 (2002) 353–358.
[32] A. Phuruangrat, D.J. Ham, S.J. Hong, S. Thongtema, J.S. Lee, J. Mater. Chem. 10 (2010) 1683–1690.
[33] Z. Gu, Y. Ma, W. Yang, G. Zhang, J. Yao, Chem. Commun. 0 (2005) 3597–3599.
[34] A.C. Marques, L. Santos, M.N. Costa, J.M. Dantas, P. Duarte, et al., Sci. Rep. 5 (2015) 9910–9917.
[35] S. Bai, K. Zhang, X. Shu, S. Chen, R. Luo, D. Li, A. Chen, CrystEngComm 16 (2014) 10210–10217.
[36] N. Dirany, M. Arab, V. Madigou, Ch Leroux, J.R. Gavarri, RSC Adv 6 (2016) 69615–69626.
[37] M. Gotic, M. Ivanda, S. Popovic, S. Music, Mater. Sci. Eng. B 77 (2000) 193–201.
[38] M.F. Daniel, B. Desbat, J.C. Lassegues, B. Gerand, M. Figlarz, J. Solid State Chem. 67 (1987) 235–247.
[39] B. Ingham, S.V. Chong, J.L. Tallon, J. Phys. Chem. B 109 (2005) 4936–4940.
[40] J. Diaz-Reyes, V. Dorantes-garcia, A. Pérez-Benitez, J.A. Balderas-Lopes, Superficies y Vacio 21 (2008) 12–17.
[41] S. Rajagopal, D. Nataraj, D. Mangalaraj, Y. Djaoued, J. Robichaud, O.Y. Khyzhun, Nanoscale Res. Lett. 4 (2009) 1335–1342.
[42] S.S. Acharyya, S. Ghosh, R. Bal, Chem. Commun. 51 (2015) 5998–6001.
[43] V.K. Singh, R.S. Tiwari, A. Srivastava, Inter. J. Mater. Scie. ISSN: 0973-4589 12 (2017).
[44] J.T. Szymansk, A.C. Roberts, Can. Mineral. 22 (1984) 681–688.
[45] C. Guéry, C. Choquet, F. Dujeancourt, J.M. Tarascon, J.C. Lassègues, J. Solid State Electrochem. 1 (1997) 199–210.
[46] L.M. Kuti, S.S. Bhella, V. Thangadurai, Inorg. Chem. 48 (2009) 6804–6811.
[47] L. Zhou, J. Zou, M. Yu, P. Lu, J. Wei, Y. Qian, Y. Wang, C. Yu, Cryst. Growth Des. 8 (2008) 3993–3998.
[48] L. Santos, J.P. Neto, A. Crespo, D. Nunes, N. Costa, I.M. Fonseca, et al., Appl. Mater. Interface 6 (2014) 12226–12234.
[49] P. Choopool, L. Sikong, K. Kooptarnond, J. Ceram. Process. Res. 17 (2016) 1230–1235.
[50] S. Songara, V. Gupta, M.K. Patra, J. Singh, L. Saini, et al., J. Phys. Chem. Solid. 73 (2012) 851–857.
[51] S. Sun, Z. Zou, G. Min, Adv. Mater. Res. 60 (2009) 16–21.
[52] H. Ren, X. Goub, Q. Yang, RSC Adv. 7 (2017) 12085–12088.
[53] R.R. Kharade, S.S. Mali, S.P. Patil, K.R. Patil, M.G. Gang, et al., Electrochim. Acta 102 (2013) 358–368.
[54] S.M. Harshulkhan, K. Janaki, G. Velraj, R.S. Ganapathy, S. Krishnaraj, J. Mater. Sci. Mater. Electron. 27 (2016) 3158–3163.
[55] F. Xu, Y. Yao, D. Bai, R. Xu, J. Mei, D. Wu, Z. Ga, K. Jiang, RSC Adv. 5 (2015) 60339–60344.
[56] P. Dong, B. Yang, C. Liu, F. Xu, X. Xi, G. Hou, R. Shao, RSC Adv 7 (2017) 947–956.
[57] D. Chen, T. Li, Q. Chen, J. Gao, B. Fan, J. Li, X. Li, R. Zhang, J. Sun, L. Gao, Nanoscale 4 (2012) 5431–5439.